ACS OMEGA

Open Access

http://pubs.acs.org/journal/acsodf

Article

Electrostatic Orientation of Optically Asymmetric Janus Particles

Mohammad Mojtaba Sadafi, Achiles Fontana da Mota, and Hossein Mosallaei*

Cite This: *ACS Omega* 2024, 9, 49172−49187

Read Online

ACCESS | Metrics & More | Article Recommendations | Supporting Information

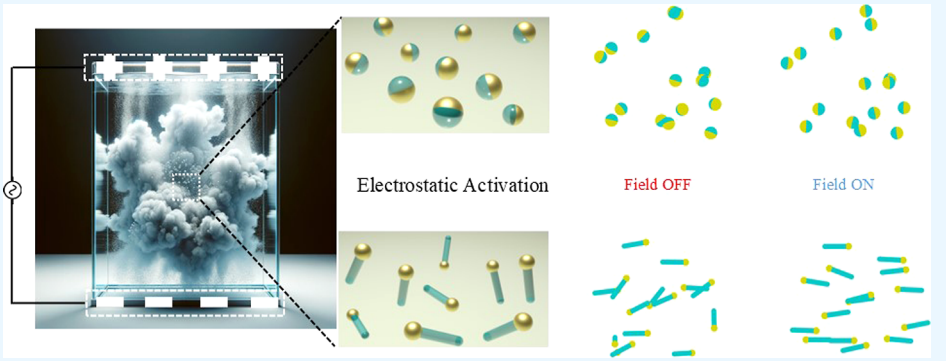

ABSTRACT: Janus micro- and nanoparticles, featuring unique dual-interface designs, are at the forefront of rapidly advancing fields such as optics, medicine, and chemistry. Accessible control over the position and orientation of Janus particles within a cluster is crucial for unlocking versatile applications, including targeted drug delivery, self-assembly, micro- and nanomotors, and asymmetric imaging. Nevertheless, precise mechanical manipulation of Janus particles remains a significant practical challenge across these fields. The current predominant methods, based on fluid flow, thermal gradients, or chemical reactions, have their precision and applicability limited by the properties of their background fluids. Therefore, this study proposes electrostatics to deliberately control the local orientation of optically asymmetric Janus particles (spherical and matchstick-like hybrid metal−dielectric objects) within a cluster to overcome the aforementioned restraints. We introduce a sophisticated multiphysics platform and employ it to explore and unveil the infrastructural physics behind the mechanical behavior of the particles when subjected to electrostatic stimuli in an ionic environment. We investigate how different deterministic and stochastic variables affect the particles' short- and long-term responses. By judicious engineering of amplitude, direction, and polarization of the external excitation, we demonstrate that the particles tend to undergo the desired rotational motion and converge to favorable orientations. The functionality of our approach is showcased in the context of an asymmetric imaging system based on optically asymmetric Janus particles. Our findings suggest a viable platform for adequate mechanical manipulation of Janus particles and pave the way for enabling numerous state-of-the-art applications in various fields.

1. INTRODUCTION

Micro- and nanoparticles are of particular interest due to the avenues that they can open toward unique applications across various research fields, including but not limited to chemistry,[1−3] biology and medicine,[4−7] and optics and photonics.[8−13] Among different particles, Janus particles, named after the Roman god Janus, possess two or more distinct physical properties on their surface, making them fascinating candidates for multifunctional applications.[14−16] Asymmetry in Janus particles can be characterized in terms of surface tension,[17] magnetic response,[18] conductivity and electrostatic charge,[19] and optical properties,[20] among other factors. To give an illustration, structural lipiodol droplets engineered with Janus particles are created by directing their self-assembly at the lipiodol−water interface, resulting in highly efficient renal embolization in rabbits.[17] Magnetic Janus photonic crystal microbeads, which display multiple fluorescence colors, are fabricated using photonic crystals, Fe_3O_4 nanoparticles, and fluorescent dyes. These microbeads are then arranged into arrays representing numbers, letters, symbols, and patterns, serving as a method for information coding and anticounterfeiting.[18] Furthermore, ultrathin electrically anisotropic Janus membranes are prepared by mixing liquid metal (LM) nanoparticles with a hydroxyethyl cellulose (HEC) suspension. These membranes exhibit excellent insulating properties on the HEC side, while the LM side allows for directly writable and conductive paths.[19] In ref 20, asymmetric particles are employed as building blocks for a nonlinear

Received: June 17, 2024
Revised: November 10, 2024
Accepted: November 15, 2024
Published: November 28, 2024

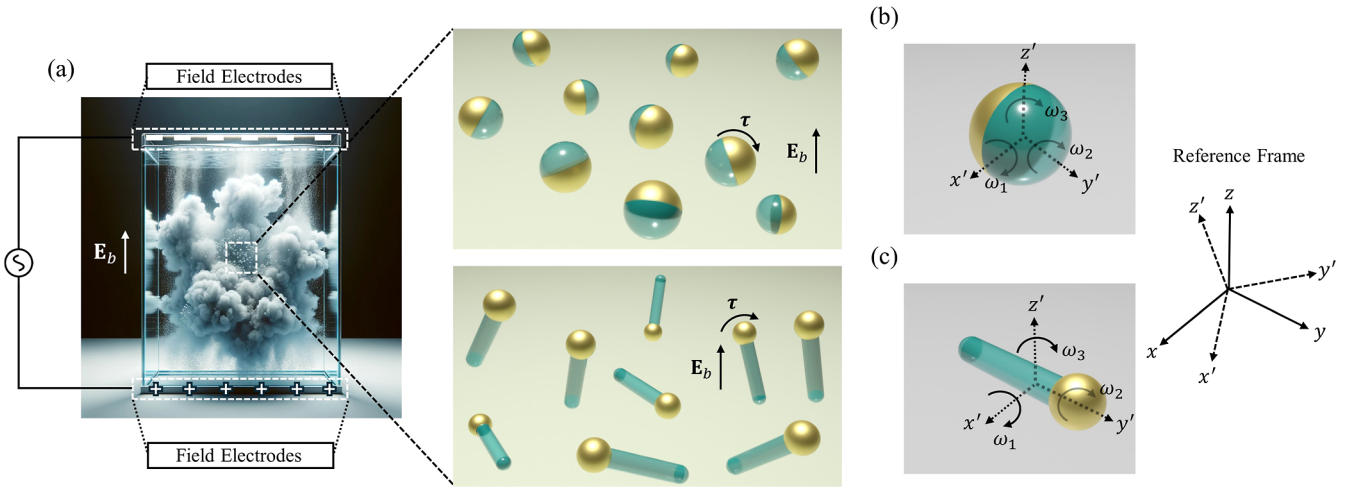

Figure 1. Illustration of a group of optically asymmetric Janus particles clustered together in an ionic solution, influenced by an external electrostatic field (a). This visualization highlights the interaction between the particles and the surrounding electrostatic environment. Schematic perspective of the spherical (b) and matchstick-like (c) Janus particles in their local coordinate systems. These representations shine a light on the geometrical structure of the particles as well as their original orientation in their local frames.

metasurface, which can produce distinct images at the third-harmonic wavelength upon illumination from opposite sides.

Asymmetric imaging is one of the distinctive applications enabled by optically asymmetric Janus particles owing to their inherent broken symmetry. Optically asymmetric Janus particles are those whose various parts of their surface are designed to interact differently with light, thereby offering properties unattainable through homogeneous particles. As a matter of fact, hybrid metal−dielectric Janus particles, both spherical and matchstick-like, are proposed, engineered, and studied as promising means of asymmetric imaging within the visible range of the electromagnetic spectrum. It is demonstrated that an adequately designed cluster of these particles is capable of providing clear vision from one side of the cluster while obscuring it from the other,[21,22] which is also referred to as the one-way cloud. However, achieving the aforementioned goal requires not only meticulous design of the particles but also precise orientation within the cluster. Consequently, an efficient and practical strategy must be introduced to manipulate and align the particles through the cloud to achieve the desired functionality.

Different approaches have been implemented to manipulate the position and direction of Janus particles, a crucial task for various applications, such as targeted drug delivery,[23,24] microscale robotics,[25,26] self-assembly and fabrication,[27,28] and asymmetric imaging.[21,22] Janus particles can be mechanically manipulated by exploiting diverse methods ranging from applying electromagnetic fields to taking advantage of mechanical waves or fluid flow.[29−32] In fact, an approach based on the optical forces resulting from the evanescent fields is introduced for the trapping and propulsion of Janus particles (spherical microspheres made of silica and half-coated with gold) along optical nanofibers. It is illustrated that hybrid Janus particles tend to experience strong localization in the transverse direction of the nanofiber and enhanced propulsion as opposed to the particles of the same size, encompassing only dielectric materials.[29] In ref 30, a hybrid propulsion method for silica Janus micromotors is introduced, utilizing an external magnetic field to fix the particles' orientation. Concurrently, an ultrasound acoustic wave induces in-plane oscillations, which can be coupled to translational motion in order to accelerate the particles toward the desired direction. Moreover, in order to examine the effects of external field frequency and particle geometry on induced force and torque, AC electric fields of various frequencies are applied to Janus particles with differing shapes (hemispherical, matchstick-like, and snowman-like) in an ionic solution.[31] The rotation and orientation of hybrid spherical Janus particles (particles consisting of dielectric and metallic hemispheres) by exploiting uniform AC electric fields are explored theoretically and evaluated by experimental techniques. Different torque contributions, including electrostatically induced dipole torque (IDT) and induced-charge-electrophoretic (ICEP) torque, are derived under the weak field assumption and investigated in terms of the field's frequency in order to shine a light on the electrokinetics of hybrid metal−dielectric Janus particles.[32] Despite all the comprehensive techniques above, the quest to predict and desirably engineer the dynamics of Janus particles in a cluster remains a challenge and a matter of active research.

Electromagnetic fields have been proven to be capable of inducing mechanical momentum in objects through different mechanisms.[33−36] Among different procedures, electrostatics falls within the most practical and reliable resources for the mechanical manipulation of particles as it can offer both efficiency and accessibility.[37−39] In particular, although highly precise methods such as asymmetry- or optically driven chemotaxis[40−42] have been used to move and orient various micro- and nanoparticles, electrostatics offers a viable approach for orienting optically asymmetric Janus particles within a reasonable time frame and independent of the background properties, which is crucial for asymmetric imaging. In order to predict the electrostatic response of electrically neutral or charged particles in an ionic solution, the Poisson−Boltzmann (PB) equation is to be solved either analytically or numerically as it governs the physics of the problem.[43−45] Although analytical solutions can be built for problems with relatively simple geometries, such as cylinders or spheres,[46,47] a rigorous numerical approach has to be implemented to solve the general case, including particles with arbitrary shapes. Various numerical techniques, such as the finite difference method (FDM)[48,49] and the finite element method (FEM),[50,51] can be utilized to solve the nonlinear PB equation. However, such

https://doi.org/10.1021/acsomega.4c05669
ACS Omega 2024, 9, 49172−49187

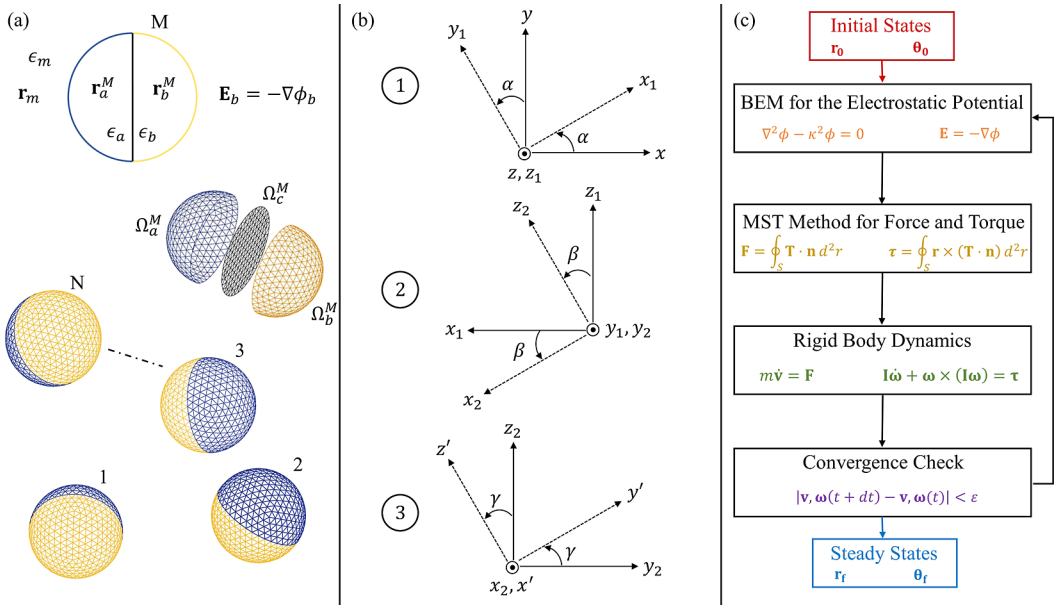

Figure 2. Schematic depiction of a cluster of N identical optically asymmetric Janus particles in an ionic background with the permittivity of ϵ_m when subjected to an electrostatic background field $\boldsymbol{E}_b = -\nabla\phi_b$ (a). The boundaries of the particles are segmented into flat triangular elements for the sake BEM analysis. Representation of the Euler angles sequence used in this paper to uniquely express the orientation of the particles in the global frame (b). Graphical summary of the multiphysics algorithm proposed in this work to capture the electrostatic and mechanical behaviors of the particles (c).

methods usually fail to address large-scale problems due to their reliance on segmenting the 3D space. In order to tackle the mentioned issue, at the cost of neglecting the nonlinear effects, a boundary element method (BEM)[52−54] can be exploited to solve the linearized PB equation, which is valid under certain assumptions, such as low potential and low ionic strength approximations.[55,56] Not only is a BEM approach efficient in terms of reducing the dimensionality of the problem by transforming the 3D problem to boundary equations, but it can also be combined with the adaptive fast multipole method (FMM) algorithms to improve the computational efficiency drastically.[57−59] Furthermore, the electrostatic behavior of the particles captured by the BEM can be rigorously coupled to their mechanical response utilizing the Maxwell stress tensor (MST) method.[60−62] The BEM can be used to obtain the electrostatic potential by solving the linearized PB equation. The MST is then employed to compute the mechanical force and torque, and eventually, the rigid body equations are solved with respect to the calculated force and torque to acquire the mechanical response of the system. The aforementioned approach can be utilized to couple electrostatics to the rigid body dynamics, taking advantage of the quaternions[63,64] to develop an insightful multiphysics platform for studying the dynamics of Janus particles in ionic media under the application of electrostatic fields.

In this sense, this work proposes electrostatics as an efficient means of mechanically manipulating a cluster of hybrid metal−dielectric Janus particles in an ionic solution, which is also referred to as activation in our paper. The configuration of the problem can be schematically seen in Figure 1. The particles under study are spherical and matchstick-like Janus particles composed of silica and gold. Such particles have been experimentally proven to enable asymmetric imaging contingent upon having the desired orientation within a cluster.[21,22] The BEM, combined with the adaptive FMM algorithm, is utilized to solve the linearized PB equation to obtain the particles' electrostatic response in a cloud. The MST method is implemented to find the force and torque imparted on the particles, and they are used as a bridge to transit from the electrostatic to the mechanical problem. The mechanical response of the particles inside the cluster is acquired by solving the rigid body dynamics equation with the help of the unit quaternions, while the impact of the background fluid is taken into account as an external Stokes force and torque. A comprehensive multiphysics platform is developed by solving the coupled linearized PB and rigid body dynamics equations simultaneously, taking into account the impacts of translational and rotational Brownian motions. The proposed platform is harnessed to study the transient and steady-state responses of isolated Janus particles under the application of electrostatic fields in various directions. The impacts of different parameters, such as the initial state of the particles, the background fluid viscosity, and the ionic solution strength on the response of both particles, are systematically computed and analyzed. By resorting to the potential energy trends of the particles, it is demonstrated that each particle has two distinct stable steady states in the orientation space, tending to choose one depending on its initial state. It is illustrated that electrostatic fields can be utilized to orient the particles within a cluster as desired. To demonstrate the effectiveness of the proposed method, multiple simulations are conducted for the cluster with various random initial states, and the results are presented in terms of probability distributions. The outcome of the simulations is exploited to assess the practicality of the particles for asymmetric imaging. It is demonstrated that the proposed method successfully aligns the particles inside the cloud in the desired direction, thereby achieving the intended objectives for various intriguing applications such as targeted drug delivery, micro- and nanomotors, and self-assembly. The rest of this paper is organized as below:

https://doi.org/10.1021/acsomega.4c05669
ACS Omega 2024, 9, 49172−49187

Section 2 briefly reviews the formalism used in developing the multiphysics platform discussed before. Section 3 summarizes our results and discussion, where isolated particles with various geometries (spherical and matchstick-like Janus particles) are analyzed in terms of the imparted torque, potential energy, and ionic solution strength. The transient and steady-state responses of the particles are also discussed concerning the viscosity of the background fluid. The orientation of the particles in a cluster with different random initial states and their functionality as an asymmetric imaging system are also investigated. Section 4 includes the concluding remarks.

2. FORMALISM

For electrically neutral particles in a nonionic medium, the Laplace equation, as described below, needs to be solved in order to predict the electrostatic response

$$\nabla^2\phi = 0 \tag{1}$$

in which ϕ is the electrostatic potential. However, in ionic media, under the low ionic strength approximation, the linearized PB equation governs the physics of the problem[55,56]

$$\nabla^2\phi - \kappa^2\phi = 0 \tag{2}$$

where $\kappa = \sqrt{\frac{8\pi e^2 I}{\epsilon_i k_B T}}$ is the Debye screening parameter,[65] accounting for the attenuation of electrostatic interactions due to the presence of ions in the solution. It should be noted that ϵ_i is the permittivity of the ionic solution, e stands for the charge of a free electron, I is the ionic strength of the aqueous solution, k_B is the Boltzmann constant, and T represents the solution temperature.

It is important to note that the proposed model in this manuscript is valid only for environments with low ionic strength and long Debye lengths, where the effects of electric body forces, such as induced charge electro-osmosis (ICEO), induced charge electrophoresis (ICEP), and dielectrophoresis (DEP), can be safely neglected (further comments on the validity of the proposed technique are provided in the Supporting Information).

For a cluster of N Spherical Janus particles placed in an ionic medium with permittivity of ϵ_m and the Debye screening parameter κ, and under the application of the background electrostatic field $\boldsymbol{E}_b = -\nabla\phi_b$ as depicted in Figure 2a, potential in each region can be expressed in terms of boundary integrals using Green's second identity as follows (a detailed description of this method can be found in the Supporting Information)

$$\phi_\iota^i(\mathbf{r}_\iota^i) = \oint_{\Omega_\iota^i+\Omega_c^i}\left({}^0G(\mathbf{r}_\iota^i,\mathbf{r}')\frac{\partial\phi_\iota^i}{\partial\mathbf{n}'}(\mathbf{r}') - \phi_\iota^i(\mathbf{r}')\frac{\partial^0 G}{\partial\mathbf{n}'}(\mathbf{r}_\iota^i,\mathbf{r}')\right)d^2r',$$
$$\iota \in \{a, b\} \text{ and } i = 1, 2, \ldots, N \tag{3}$$

$$\phi_m(\mathbf{r}_m) = \sum_{i=1}^{N}\left[\oint_{\Omega_a^i+\Omega_b^i}\left(\phi_m(\mathbf{r}')\frac{\partial^\kappa G}{\partial\mathbf{n}'}(\mathbf{r}_m,\mathbf{r}') - {}^\kappa G(\mathbf{r}_m,\mathbf{r}')\frac{\partial\phi_m}{\partial\mathbf{n}'}(\mathbf{r}')\right)d^2r'\right] + \phi_b(\mathbf{r}_m) \tag{4}$$

where $\phi_\iota^i(\mathbf{r}_\iota^i)$ shows the potential inside the dielectric (ι = a) or metallic (ι = b) part of the ith particle, $\phi_m(\mathbf{r}_m)$ is the total potential in the background, Ω represents the boundary, $\mathbf{n}$ is the outward unit normal vector to each boundary, and ${}^\kappa G(\mathbf{r}, \mathbf{r}')$ is the Green's function of the linearized PB equation given by[66]

$${}^\kappa G(\mathbf{r},\mathbf{r}') = \frac{e^{-\kappa|\mathbf{r}-\mathbf{r}'|}}{4\pi|\mathbf{r}-\mathbf{r}'|} \tag{5}$$

which can be reduced to the Green's function of the Laplace equation by setting $\kappa = 0$.

By letting the position vectors approach the boundaries in eqs 3 and 4 and applying the following boundary conditions on the surface of the ith particle, a system of boundary integral equations can be derived

$$\begin{cases}\phi_a^i(\mathbf{r}_{\Omega_a^i}) = \phi_m(\mathbf{r}_{\Omega_a^i}),\\ \epsilon_a\dfrac{\partial\phi_a^i}{\partial\mathbf{n}}(\mathbf{r}_{\Omega_a^i}) = \epsilon_m\dfrac{\partial\phi_m}{\partial\mathbf{n}}(\mathbf{r}_{\Omega_a^i}),\end{cases}$$
$$\begin{cases}\phi_b^i(\mathbf{r}_{\Omega_b^i}) = \phi_m(\mathbf{r}_{\Omega_b^i}),\\ \epsilon_b\dfrac{\partial\phi_b^i}{\partial\mathbf{n}}(\mathbf{r}_{\Omega_b^i}) = \epsilon_m\dfrac{\partial\phi_m}{\partial\mathbf{n}}(\mathbf{r}_{\Omega_b^i}),\end{cases}$$
$$\begin{cases}\phi_a^i(\mathbf{r}_{\Omega_c^i}) = \phi_b^i(\mathbf{r}_{\Omega_c^i}),\\ \epsilon_a\dfrac{\partial\phi_a^i}{\partial\mathbf{n}}(\mathbf{r}_{\Omega_c^i}) = \epsilon_b\dfrac{\partial\phi_b^i}{\partial\mathbf{n}}(\mathbf{r}_{\Omega_c^i}),\end{cases} \tag{6}$$

where ϵ_a represents the permittivity of the dielectric part, and ϵ_b stands for the permittivity of the metal. After discretizing the surface of each particle into L flat triangular elements and assuming a constant potential over the area of each triangle, the boundary integral equations can be reduced to a matrix equation described as follows

$$\mathrm{A}x = \mathbf{b} \tag{7}$$

in which $\mathbf{A}$ is a square matrix of rank 2NL, known as the interaction matrix, $\mathbf{x}$ is the 2NL × 1 vector of unknowns on the boundaries to be determined, and $\boldsymbol{b}$ is the excitation vector of the same dimensions as $\mathbf{x}$, dictated by the background electrostatic field. The interaction matrix can be divided into block matrices as shown below

$$\mathbf{A} = \begin{bmatrix}\mathbf{A}^d & \mathbf{A}^{12} & \ldots & \mathbf{A}^{1N}\\ \mathbf{A}^{21} & \mathbf{A}^d & \ldots & \mathbf{A}^{2N}\\ \vdots & \vdots & \ddots & \vdots\\ \mathbf{A}^{N1} & \mathbf{A}^{N2} & \ldots & \mathbf{A}^d\end{bmatrix} \tag{8}$$

where $\mathbf{A}^d$ is the self-interaction matrix calculated using the boundary integrals, and $\mathbf{A}^{ij}$ denotes the cross-interaction matrix, which can be effectively calculated employing the adaptive FMM algorithm[57−59] (refer to the Supporting Information for the calculation details). The vector of unknowns is defined as $\mathbf{x} = [\tilde{\mathbf{x}}^1, \tilde{\mathbf{x}}^2, \ldots, \tilde{\mathbf{x}}^N]^\dagger$ with

https://doi.org/10.1021/acsomega.4c05669
ACS Omega 2024, 9, 49172−49187

$$\tilde{\mathbf{x}}^i = \left[\phi_a^i(\mathbf{r}_{\Omega_a^i}),\ \frac{\partial \phi_a^i}{\partial \mathbf{n}}(\mathbf{r}_{\Omega_a^i}),\ \phi_b^i(\mathbf{r}_{\Omega_b^i}),\ \frac{\partial \phi_b^i}{\partial \mathbf{n}}(\mathbf{r}_{\Omega_b^i}),\ \phi_a^i(\mathbf{r}_{\Omega_a^i}),\ \frac{\partial \phi_a^i}{\partial \mathbf{n}}(\mathbf{r}_{\Omega_a^i})\right]^\dagger \tag{9}$$

while the excitation vector can be described as $\mathbf{b} = [\tilde{\mathbf{b}}^1, \tilde{\mathbf{b}}^2, ..., \tilde{\mathbf{b}}^N]^\dagger$ with

$$\tilde{\mathbf{b}}^i = [\mathbf{0},\ \phi_b(\mathbf{r}_{\Omega_a^i}),\ \mathbf{0},\ \phi_b(\mathbf{r}_{\Omega_b^i}),\ \mathbf{0},\ \mathbf{0}]^\dagger \tag{10}$$

After solving eq 7 utilizing the generalized minimal residual method (GMRES), the electric field can be obtained as $\mathbf{E} = -\nabla\phi$, which can then be exploited to compute the Maxwell stress tensor (MST) in the ionic medium as follows[60,61]

$$\mathbf{T} = \epsilon_0\epsilon_m \mathbf{E} \otimes \mathbf{E} - \frac{1}{2}\epsilon_0\epsilon_m(|\mathbf{E}|^2 + \kappa^2\phi^2)\bar{\mathbf{I}} \tag{11}$$

In which ϵ_0 expresses vacuum permittivity, and $\bar{\mathbf{I}}$ is the unit dyadic. Having defined the proper MST, the force and torque imparted on each Janus particle can be calculated as given below

$$\mathbf{F}^i = \oint_{\Omega_a^i+\Omega_b^i} \mathbf{T}\cdot\mathbf{n}\ \mathrm{d}^2r' \tag{12}$$

$$\boldsymbol{\tau}^i = \oint_{\Omega_a^i+\Omega_b^i} (\mathbf{r}' - \mathbf{r}_{cm}^i) \times (\mathbf{T}\cdot\mathbf{n})\ \mathrm{d}^2r' \tag{13}$$

where $\mathbf{r}_{cm}^i$ shows the center of mass of the ith particle. Therefore, the calculated force and torque can be utilized to predict the position and orientation of the particles through solving the rigid body dynamics equations as follows

$$\mathbf{F}^i + \mathbf{R}_d^i(t) = m^i\frac{\partial \mathbf{v}^i}{\partial t} + \bar{\bar{\boldsymbol{\mu}}}_d\mathbf{v}^i \tag{14}$$

$$\boldsymbol{\tau}^i + \mathbf{R}_r^i(t) = \mathbf{I}^i\frac{\partial \boldsymbol{\omega}^i}{\partial t} + \boldsymbol{\omega}^i \times (\mathbf{I}^i\boldsymbol{\omega}^i) + \bar{\bar{\boldsymbol{\mu}}}_r\boldsymbol{\omega}^i \tag{15}$$

in which m^i is the mass of the ith particle, $\mathbf{v}^i$ is its transnational velocity, $\mathbf{I}^i$ stands for its moment of inertia tensor, and $\boldsymbol{\omega}^i$ denotes its angular velocity. It is worth noting that $\bar{\bar{\boldsymbol{\mu}}}_d$ and $\bar{\bar{\boldsymbol{\mu}}}_r$ are the translational and rotational viscous damping tensors,[32] respectively, while $\mathbf{R}_d^i(t)$ and $\mathbf{R}_r^i(t)$ are stochastic terms accounting for the Brownian motion of the particles.[67−70]

In order to simultaneously solve eqs 14 and 15, a set of Euler angles, as shown in Figure 2b, are used to determine the orientation of the particle's frame ($x'y'z'$) with respect to the global frame (xyz). Moreover, a unit quaternion[71] $\mathbf{q}^i = [q_1^i, q_2^i, q_3^i, q_4^i]^\dagger$ ($\|\mathbf{q}^i\|_2 = 1$) is introduced to track the trajectory of the Euler angles over the course of time, obeying the following differential equation

$$\frac{\partial \mathbf{q}^i}{\partial t} = \frac{1}{2}\begin{bmatrix} 0 & \omega_3^i & -\omega_2^i & \omega_1^i \\ -\omega_3^i & 0 & \omega_1^i & \omega_2^i \\ \omega_2^i & -\omega_1^i & 0 & \omega_3^i \\ -\omega_1^i & -\omega_2^i & -\omega_3^i & 0 \end{bmatrix}\begin{bmatrix} q_1^i \\ q_2^i \\ q_3^i \\ q_4^i \end{bmatrix} \tag{16}$$

which can be solved concurrently with eqs 14 and 15 to uniquely determine the position and orientation of each particle using a sufficiently small time step. The multiphysics platform proposed in this paper can be summarized as follows:

1. Random initial values are assigned to the position, velocity, orientation, and angular velocity of each particle.
2. The BEM is employed to solve the linearized PB equation to obtain the electrostatic potential.
3. The imparted force and torque are acquired by integrating the MST on the boundary of each particle.
4. Rigid body dynamics equations are solved by exploiting a reasonable time step in order to update the position and orientation of each particle.
5. A convergence test is performed to check whether the steady state is achieved or not.
6. If the convergence criteria are not satisfied, the algorithm returns to step 2.

The aforementioned multiphysics algorithm is schematically summarized in Figure 2c (comments on the validity of the proposed platform can be found in the Supporting Information).

3. RESULTS AND DISCUSSION

3.1. Dynamics of an Isolated Janus Particle. This section aims to provide insight into the electrostatic and mechanical responses of an isolated optically asymmetric Janus particle in an ionic solution, particularly under the application of external electrostatic stimulation. The particles under investigation are spherical and matchstick-like Janus particles, as illustrated in Figure 1b,c, respectively. The geometrical dimensions of the particles are chosen to optimize asymmetric imaging performance.[21] The spherical Janus particle is engineered to have a diameter of d = 180 nm, while the matchstick-like particle consists of a cylindrical rod with dimensions d_1 = 0.29 μm (diameter) and h = 1.195 μm (length), as well as a spherical cap with a diameter of d_2 = 0.4 μm.

The particles are hybrid metal−dielectric, with the dielectric part considered to be silica with a permittivity of ϵ_a = 3.9, and the metallic section assumed to be gold with an ideal permittivity of $\epsilon_b = \infty$. The mass densities are considered ρ_{silica} = 2650 kg/m^3 and ρ_{gold} = 19300 kg/m^3 for silica and gold, respectively. These particles are immersed in a background medium with permittivity ϵ_m ranging from ϵ_{air} = 1 for air to ϵ_{water} = 80 for water. In this section, the particles are assumed to lie in the yz-plane of the reference frame ($\alpha = \beta = 0$) for the sake of simplicity in analysis, without loss of generality, as this condition can always be satisfied by resorting to proper coordinate transformations. The applied electrostatic field is presumed to have the form $\mathbf{E}_b = E_0(\sin\theta_0\hat{a}_y + \cos\theta_0\hat{a}_z)$, where E_0 represents the electric field amplitude in units of

https://doi.org/10.1021/acsomega.4c05669
ACS Omega 2024, 9, 49172−49187

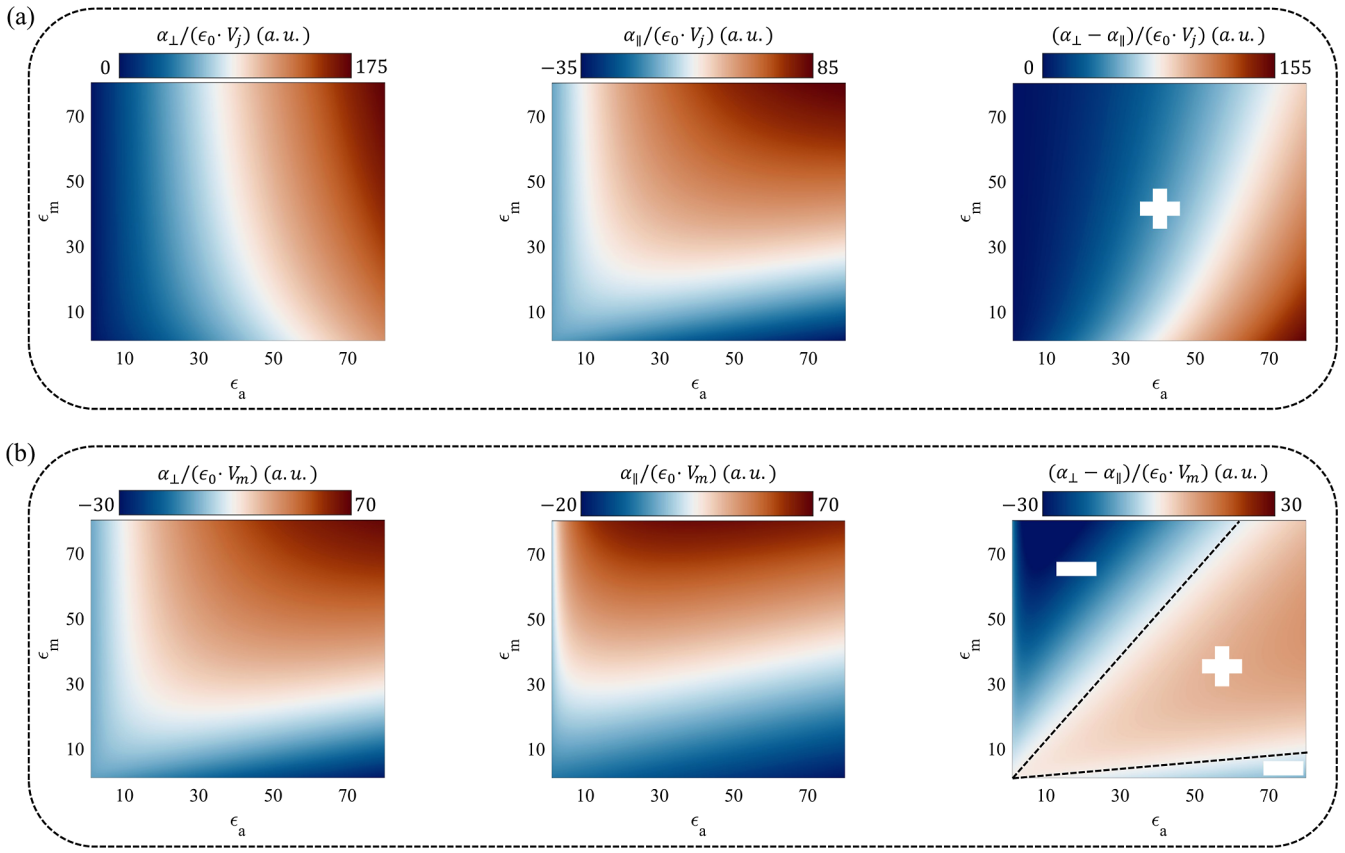

Figure 3. Perpendicular and parallel electric dipole polarizabilities of the spherical Janus particle, along with their difference, calculated for various permittivity values of the dielectric section and the background (a). Perpendicular and parallel polarizability values of the matchstick-like Janus particle, as well as their difference, as a function of the dielectric section and background permittivity values (b). This figure illustrates the behavior of the studied Janus particles in an electrostatic field.

V/m, and θ_0 describes its direction. It is worth noting that throughout the rest of this section, the motion of the particles is considered deterministic ($\mathbf{R}_d(t) = \mathbf{R}_r(t) = \mathbf{0}$), with the emphasis placed on deriving the electrostatic and mechanical characteristics of the particles.

The electrostatic response of an optically asymmetric Janus particle in a uniform electrostatic field can be effectively described using its anisotropic electric dipole polarizability tensor.[72,73] Therefore, the electric dipole moment of the particle can be obtained as follows

$$\mathbf{p} = \overline{\overline{\alpha}}\mathbf{E} \tag{17}$$

in which $\overline{\overline{\alpha}}$ is the polarizability tensor in the particle's local coordinates, defined as follows

$$\overline{\overline{\alpha}} = \begin{bmatrix} \alpha_\perp & 0 & 0 \\ 0 & \alpha_\parallel & 0 \\ 0 & 0 & \alpha_\perp \end{bmatrix} \tag{18}$$

It should be noted that $\alpha_\parallel$ is the polarizability along the anisotropy axis of the particle, while $\alpha_\perp$ represents the polarizability along an axis perpendicular to the anisotropy direction. Therefore, a uniform in-plane electrostatic field with an amplitude of E_0 in the local coordinates of the particle can be expressed as

$$\mathbf{E} = E_0(-\sin\theta\hat{a}_\parallel + \cos\theta\hat{a}_\perp) \tag{19}$$

where $\hat{a}_\parallel$ and $\hat{a}_\perp$ are the in-planes unit vectors parallel and perpendicular to the anisotropy axis, respectively, and θ determines the complement of the angle between the applied electrostatic field and the anisotropy direction of the particle. Therefore, the imparted electrostatic torque on the particle can be obtained as follows

$$\boldsymbol{\tau} = \mathbf{p} \times \mathbf{E} = -\frac{1}{2}(\alpha_\perp - \alpha_\parallel)\sin 2\theta\hat{a}_o \tag{20}$$

In which $\hat{a}_o$ is a unit vector pointing out-of-plane.

For both the spherical and matchstick-like Janus particles, the perpendicular and parallel polarizabilities, along with their difference, are calculated for various permittivity values of the dielectric section and the background. This provides insight into their response under an applied electrostatic field. The results are normalized by the factor $F_n = \epsilon_0 \cdot V_p$ for improved scalability and illustrated in Figure 3. As clearly shown in Figure 3a, although the perpendicular and parallel electric dipole polarizabilities follow different trajectories, their difference remains positive in all scenarios. This can be attributed to the simple geometry of the spherical Janus particles, where the combined contributions of the two equally distributed dielectric and metallic hemispheres consistently result in a perpendicular polarizability greater than the parallel one, leading to a positive difference. On the contrary, as can be seen from Figure 3b, the perpendicular and parallel polarizability values of the matchstick-like Janus particle can be meticulously controlled to result in either positive or negative difference

https://doi.org/10.1021/acsomega.4c05669
ACS Omega 2024, 9, 49172−49187

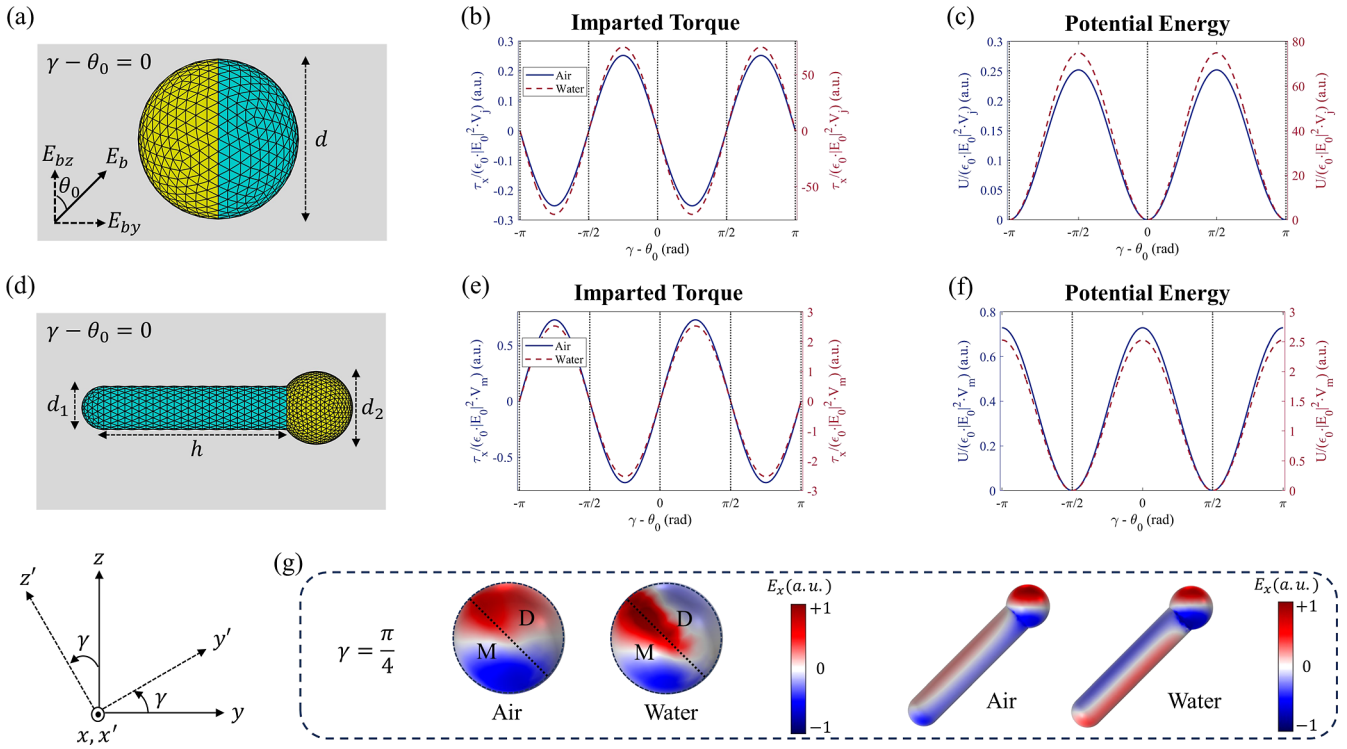

Figure 4. Cross sections of the spherical (a) and matchstick-like (d) Janus particles in the *yz*-plane of the global frame as well as their corresponding geometrical parameters. Imparted torques at different orientation angles (γ) in air and water backgrounds for the spherical (b) and matchstick-like (e) Janus particles. Corresponding potential energies $\tau_x = -\nabla U$ of the spherical (c) and matchstick-like (f) particles in air and water backgrounds. Zero-crossings of the torque and potential curves, indicated by vertical dashed lines, are associated with equilibrium and stable equilibrium points, respectively. Out-of-plane component of the electric field for both particle types at $\gamma = \frac{\pi}{4}$ in air and water backgrounds (g). These electric fields demonstrate the change in the polarization of the dielectric parts of the particles in different background materials.

values. This behavior can be traced back to its more complex geometry, where the dielectric and metallic sections are unequally distributed. The difference between the perpendicular and parallel polarizabilities is particularly important, since its sign directly contributes to the stable steady states of the particles in orientation space.

The imparted electrostatic torques on the spherical Janus particle around the *x*-axis of the reference frame are depicted in Figure 4a for both air and water background media. The results presented herein are generated under the assumption of nonionic solution with $\kappa = 0$ and are normalized to the factor $F_n = \epsilon_0 \cdot |E_0|^2 \cdot V_p$, where V_p is the volume of the particle under study, to facilitate scalability. The effects of ionic strength on the response of the particles will be examined subsequently. As can be observed, the imposed torques exhibit periodic behaviors, which can be anticipated by the inherent rotational symmetry of the particle around the *x*-axis under the applied electrostatic field. Besides, the imparted torques express sinusoidal shapes of the form $\tau_x = \tau_0 \sin(2\gamma - 2\theta_0)$, resembling the dipolar nature of the particle.[31,32] Also, due to the stronger interaction with the background field (translating to higher polarizability), the particle tends to experience a greater torque in water than in free space.

The equilibrium points are defined as the zero-crossings of the torque curves, as demonstrated by the vertical dashed lines in Figure 4b. It can be observed that there are various equilibrium points in each cycle, at which the particle does not tend to undergo any rotational motion. The equilibrium points for the spherical Janus particle in both air and water backgrounds include $\gamma - \theta_0 = 0, \frac{\pi}{2}$, and π. Although the induced torque has multiple equilibrium points, only the stable equilibrium points represent steady states in the solution space. A stable equilibrium point is defined as a state in the solution space, at which the particle tends to return to its initial state in case of any deviation. The stability of the equilibrium points can be investigated in terms of the potential energy of the spherical Janus particle. Due to the conservative nature of the electrostatic torque, it can be described using a potential as $\tau_x = -\nabla U$, which is calculated and shown in Figure 4c for air and water backgrounds. The stable equilibrium points correspond to the minima of the potential energy curves, which in the cases of air and water backgrounds are $\gamma - \theta_0 = 0$ and π. Consequently, there exist two distinct stable steady states in the solution space, implying that the final state of the particle is strictly dependent on its random initial conditions. The impacts of this randomness will be discussed in detail later on.

The normalized torque curves for the matchstick-like Janus particle in air and water backgrounds are depicted in Figure 4e under the same assumptions as for the spherical Janus particle. It is evident that the imparted torques exhibit periodicity in this case as well, following the inherent symmetry of the problem. Moreover, the induced torques are sinusoidal waveforms owing to the dipolar nature of the particle, with a stronger amplitude in water rather than air due to the intensified polarization in water. The observed equilibrium points for both air and water backgrounds are located at $\gamma - \theta_0 = 0, \frac{\pi}{2}$, and π, similar to the spherical Janus particle. Nonetheless, as evident in Figure 4f, the potential energy approaches its minima at $\gamma - \theta_0 = \frac{\pi}{2}$ and $-\frac{\pi}{2}$. Therefore, the

https://doi.org/10.1021/acsomega.4c05669
ACS Omega 2024, 9, 49172−49187

stable equilibrium points for the matchstick-like Janus particle can be considered complementary to those of the spherical particle. In conclusion, the particles will align in the direction of the highest polarizability, which can be determined by the sign of the difference between the perpendicular and parallel polarizabilities.

To elucidate the performance of the particles in both air and water backgrounds, the out-of-plane component of the electric field at $\gamma = \pi/4$ is depicted for both the spherical and matchstick-like Janus particles in Figure 4g. As can be observed, the metallic parts for both particle types are polarized in the opposite direction of the applied electrostatic field. Nevertheless, the dielectric sections exhibit different behaviors depending on the background contrast. While the dielectric segments of both particles tend to polarize in the opposite orientation to the applied field in free space, this trend no longer holds in water. Due to the high polarizability of the background in water, the dielectric parts are polarized in the same direction as the background field, as opposed to the metallic sections. The total imparted torque on the particles can be considered as the superposition of the torques induced on the dielectric and metallic parts. Consequently, as the background contrast is capable of amplifying the polarizability as well as changing its sign, the behavior of the imparted torques is expected to vary with respect to the background permittivity.

For the sake of clarity, the normalized amplitudes of the imparted torques for the spherical and matchstick-like Janus particle with respect to the background permittivity are depicted in Figure 5a,b, respectively. The demonstrated results are generated for various ionic strengths of the background medium in order to shine a light on the impacts of potential screening (damped electrostatic interaction) caused by the ions. As illustrated, the induced torques tend to diminish as the salt concentration increases. The mentioned behavior is a direct consequence of damped electrostatic interactions in the ionic medium, occurring because of the energy absorbed by the continuum of ions.[74,75] On the other hand, extra attention must be paid when interpreting the trend of the torque while changing the background permittivity. As mentioned earlier, the induced torque on the particles can be supposed as the superposition of the torque imparted on the dielectric and metallic parts. It can be clearly seen in Figure 5a that the driving torque on the spherical Janus particle climbs monotonically as the permittivity of the background increases. Given that the spherical Janus particle exhibits maximum asymmetry with half dielectric and half metal composition, the torque will primarily be dictated by the metallic part. This dominance holds true regardless of the background permittivity, as the torque generated by the metallic part tends to be stronger than that generated by the dielectric part. On the contrary, the matchstick-like Janus particle is not maximally asymmetric, resulting in unequal contributions from the dielectric and metallic sections to the total induced torque. Consequently, as illustrated in Figure 5b, the torque changes sign with increasing permittivity of the background, indicating that the dominant contribution can shift from metallic to dielectric in some regions. This asymmetry of the matchstick-like Janus particle can be leveraged as a valuable parameter in the design paradigm to achieve the desired behavior, as the sign of the torque directly affects the stable equilibrium points.

Having obtained the torques imposed on the Janus particles as well as the associated stable equilibrium points, the

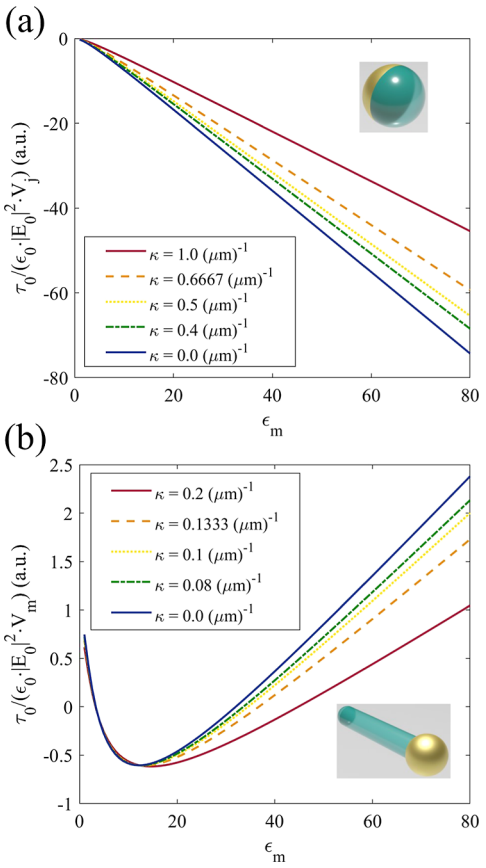

Figure 5. Imparted torque amplitudes as a function of the background permittivity for the spherical (a) and matchstick-like (b) Janus particles in ionic solutions with varying Debye parameters. These graphs shine a light on the impacts of salt concentration and background polarizability on the induced torques for various particle types.

rotational motion trajectories for both particles in air and water backgrounds are calculated for a background field polarized in the z-direction of the reference frame ($\theta_0 = 0$). The background media are considered to be nonionic ($\kappa = 0$), as the impact of the ions can be modeled as a linear scale applied to the induced torques. For the spherical Janus particle, the rotational viscous damping constants are chosen to be $\mu_{r,air} = 9.1608 \times 10^{-28}$ N m s and $\mu_{r,water} = 8.1543 \times 10^{-25}$ N m s for air and water backgrounds, respectively (these values are calculated based on Stokes flow approximations given in the Supporting Information). The amplitude of the applied electrostatic field is assumed to be $E_0 = 5 \times 10^4$ V/m, which guarantees convergence within a reasonable time frame. Starting from a random initial state, the rotational motion trajectories of the spherical Janus particle in air and water backgrounds are demonstrated in Figure 6a. As can be observed, in free space, the trajectory is of an under-damped nature, as opposed to water background, in which the particle undergoes an overdamped motion. The contrast in motions originates from the fact that the particle experiences a much more immense viscous damping in a fluid rather than a gas. Moreover, due to the nonlinear nature of the problem, the steady state of the particle is not unique and must be determined with respect to its initial state. Therefore, Figure 6b introduces a mapping from the initial (γ_0) to steady states

https://doi.org/10.1021/acsomega.4c05669
ACS Omega 2024, 9, 49172−49187

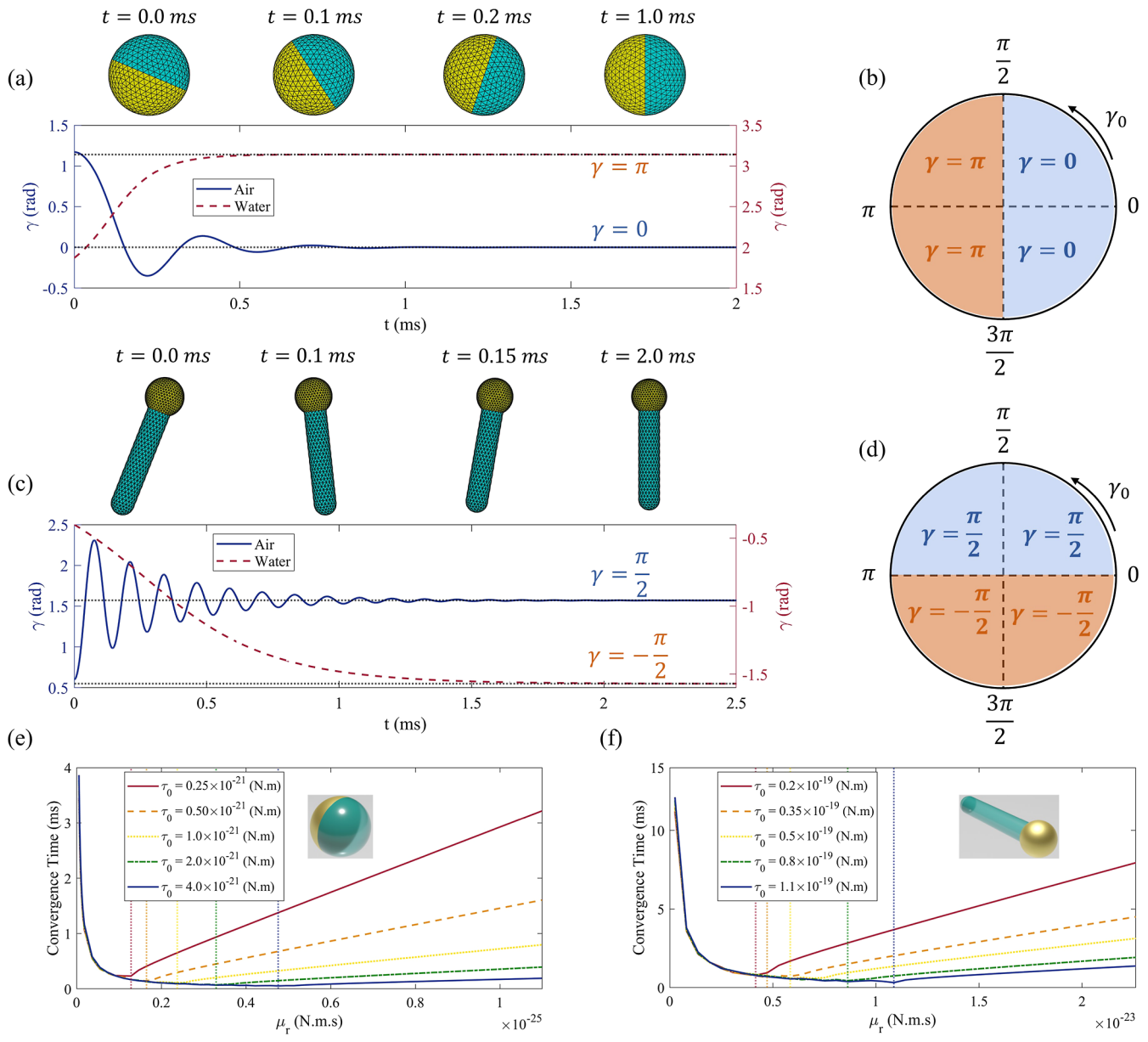

Figure 6. Rotational motion trajectories in air and water backgrounds for the spherical (a) and matchstick-like (c) Janus particles under the application of an electrostatic field parallel to the *z*-axis of the global coordinate system. These visualizations show that the particles tend to choose various steady states considering their initial states. Mappings from the initial to steady states of the spherical (b) and matchstick-like (d) particles. These mappings can be used to predict the final alignment angle of the particles subject to their initial angles. Convergence time of the spherical (e) and matchstick-like (f) Janus particles as a function of rotational viscous damping and for different applied torques. The vertical dashed lines represent critically damped oscillations. These curves can be used to control the mechanical response of the particles in different background materials.

(γ) of the spherical Janus particle, clarifying the procedure for defining the final state of the particle.

Moreover, the rotational motions of the matchstick-like Janus particle are illustrated in Figure 6c for both air and water backgrounds over the course of time. The background electrostatic field has an amplitude of $E_0 = 5 \times 10^5$ V/m, and the viscous damping constants are $\mu_{r,air} = 8.796 \times 10^{-25}$ N m s and $\mu_{r,water} = 2.764 \times 10^{-22}$ N m s for air and water backgrounds, respectively. It should be noted that the hydrodynamic resistance of the matchstick-like Janus particle is generally tensorial in nature due to its inherent anisotropy. However, since the primary focus of this manuscript is to capture the steady-state response of the particles, we assume the hydrodynamic resistance to be identical in all directions for the sake of simplicity. As can be seen, similar to the spherical Janus particle, the matchstick-like particle experiences an under-damped rotational motion in free space, while the rotational motion in water demonstrates an overdamped behavior owing to the significantly higher rotational viscous damping. Due to the nonlinearity of the problem, there are two stable steady-states in the solution space, among which the particle tends to choose one considering its initial state. The initial state of the particle can be mapped to its final state by resorting to the mapping illustrated in Figure 6d. It should be noted that the rotational motion of both spherical and matchstick-like Janus particles are guaranteed to be stable

https://doi.org/10.1021/acsomega.4c05669
ACS Omega 2024, 9, 49172−49187

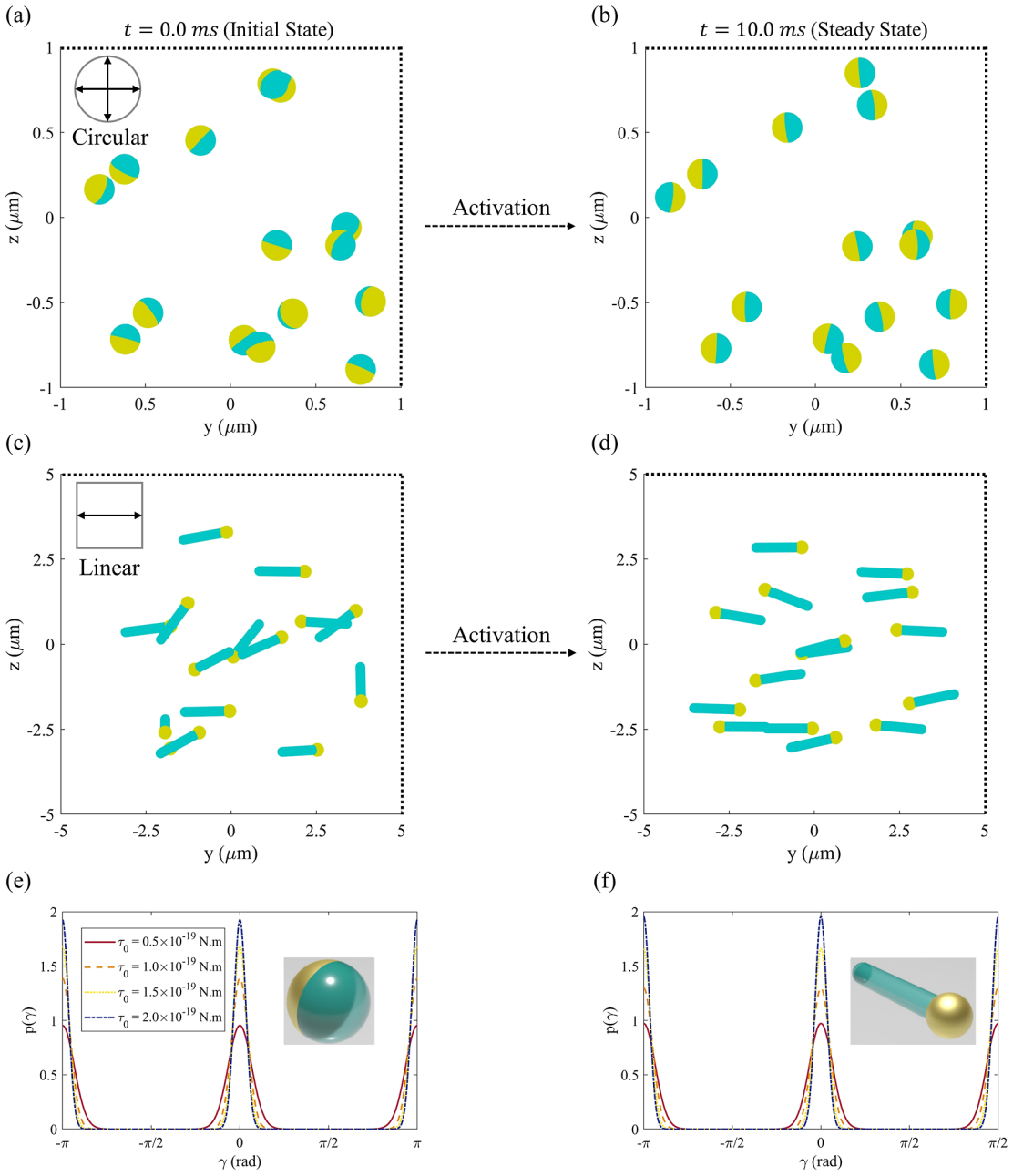

Figure 7. Initial (a) and final (b) states of a cluster of 15 spherical Janus particles in air exposed to a circularly polarized background electric field in the *yz*-plane of the global coordinates. Starting (c) and steady states (d) of a group of 15 matchstick-like Janus particles in air under a linearly polarized background electric field in the *yz*-plane of the global frame. These figures demonstrate that electrostatic fields can be utilized to orient the particles to the desired angles. Probability distributions of the *yz*-plane alignment angle γ for the spherical (e) and matchstick-like (f) particles in air under various applied torque amplitudes. These curve can be used to interpret the stochastic behavior of the steady states of different particle types.

contingent upon a nonzero rotational viscous damping constant ($\mu_r \neq 0$). However, the time it takes for the particle to reach the steady state, also referred to as the convergence time, depends on both the strength of the applied field and background damping, which should be studied carefully.

Due to the nonlinear nature of the motion equations, the response of each particle not only depends on the rotational viscous damping constant (μ_r) of the background but also varies as a function of the strength of the applied electrostatic field. In order to elaborate on the impacts of different parameters on the convergence of the particles, the convergence time for various induced torque amplitudes is plotted with respect to the rotational viscous damping of the background for both spherical and matchstick-like Janus particles in Figure 6e,f, respectively. As can be clearly inspected, the convergence time for both particles approaches infinity asymptotically as the damping of the background tends toward zero, corresponding to the undamped scenario. By increasing the rotational viscous damping of the background, the convergence time tends to drop in the under-damped regime until it reaches its minimum, which is also referred to as the critically damped oscillator. The critically damped points for both particles subject to different imparted torques are marked using vertical dashed lines in Figure 6e,f. Exceeding the

https://doi.org/10.1021/acsomega.4c05669
ACS Omega 2024, 9, 49172−49187

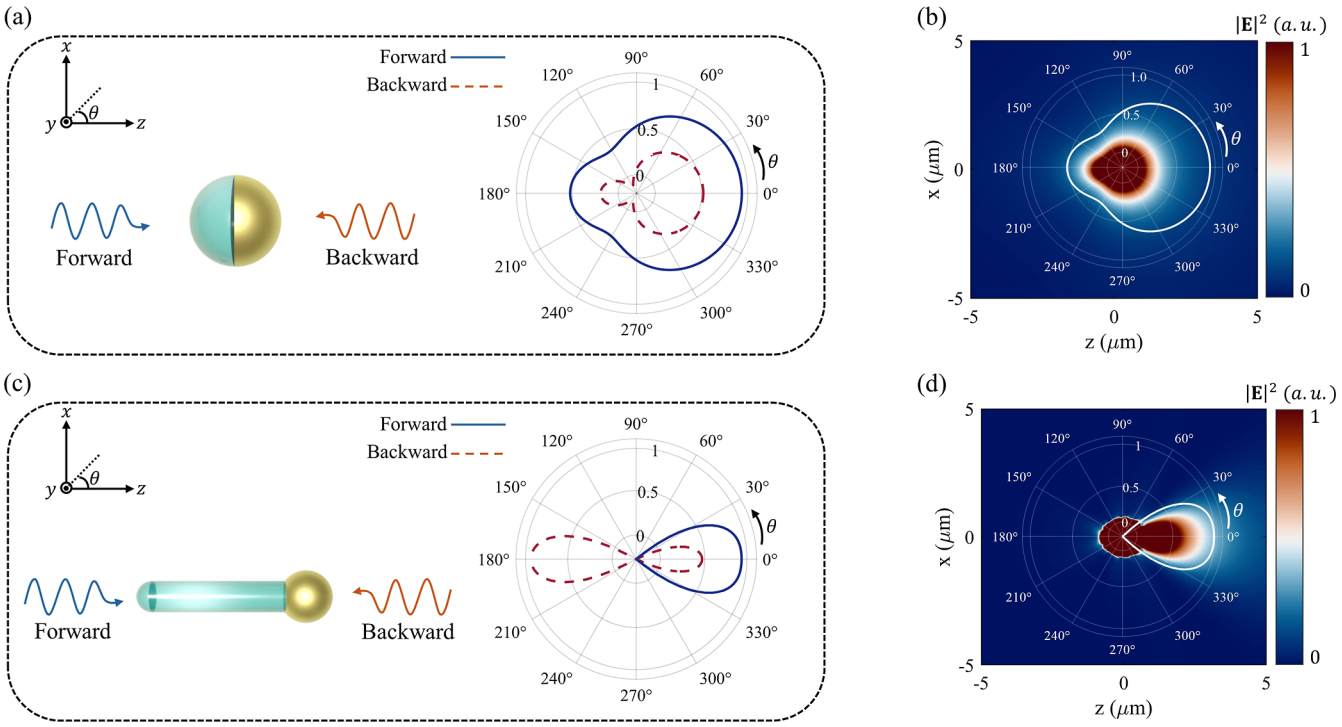

Figure 8. Far-field gain of the spherical Janus particle when illuminated from different sides (a). Electric field distribution and far-field gain of the spherical Janus particle under forward illumination (b). Far-field gain of the matchstick-like Janus particle calculated for both forward and backward scenarios (c). Electric field pattern and far-field gain of the matchstick-like Janus particle for the forward scenario (d). This figure highlights the asymmetric scattering characteristics of the Janus particles studied in this manuscript.

critically damped point, the convergence time begins to increase in the overdamped realm. It can be observed that based on the background's properties, a pertinent applied torque always exists, ensuring the system is at the critically damped point. Therefore, the background field is able to be engineered accordingly to acquire the desired convergence time. The aforementioned characteristics of the isolated particles can be exploited to orient them in a cluster containing many particles to obtain the desired functionalities.

3.2. Orientation of the Particles in a Cluster and Asymmetric Imaging. In this section, in order to elaborate on the orientation of a cluster of optically asymmetric Janus particles, electrostatic fields with various attributes are applied to the random initial distributions of both the spherical and matchstick-like Janus particles in a cluster. Their behaviors are then observed and investigated in the steady state. All the studied systems are considered to be at room temperature (T = 300 K), and the impacts of Brownian translational and rotational motions are taken into account by following the fluctuation−dissipation theorem.[76,77] This is achieved by assuming $\mathbf{R}_{\mathrm{d}}^{i}(t) = \sqrt{2k_{\mathrm{B}}T\mu_{\mathrm{d}}}\,\mathbf{\Gamma}_{\mathrm{d}}^{i}(t)$ and $\mathbf{R}_{\mathrm{r}}^{i}(t) = \sqrt{2k_{\mathrm{B}}T\mu_{\mathrm{r}}}\,\mathbf{\Gamma}_{\mathrm{r}}^{i}(t)$ for translational and rotational motions, respectively. Here, k_{B} stands for the Boltzmann constant, and $\Gamma_{\mathrm{r}}^{i}(t)$ and $\Gamma_{\mathrm{r}}^{i}(t)$ represent standard Wiener processes,[67−69] accounting for the random walk of the particles. It is worth noting that, similar to the hydrodynamic resistance of the matchstick-like Janus particle, its Brownian motion is also tensorial. However, for simplicity, it is assumed to be identical in all directions, as the primary focus is on calculating the final states of the particles. We handle the collisions between the particles by resorting to the hard-sphere approximation (refer to the Supporting Information for further details on the method). It should be noted that for the sake of simplicity, a nonionic background is considered in the rest of this section (κ = 0), as the impact of salt can be modeled by a linear scale of the applied torque.

For the spherical Janus particles, considering their dimensions, a random initial distribution of 15 particles is examined in air, enclosed within a cubic box with a side length of d_{b} = 2 μm, as illustrated in Figure 7a. The applied background field is assumed to take the form $\mathbf{E}_{\mathrm{b}} = E_0(\cos(\omega_{\mathrm{b}}t)\hat{a}_x + \sin(\omega_{\mathrm{b}}t)\hat{a}_z)$, representing a circular polarization state. The selection of a circularly polarized background field corresponds to the requirement that the particles should be manipulated to align within the yz-plane of the global coordinates. Consequently, it is necessary not only to control the particles within the yz-plane but also to deliberately monitor their angles in the xz-plane to ensure the achievement of the desired steady state. Therefore, the circular polarization provides an electric field that rotates in the xz-plane of the global coordinates, causing the particles to align in the yz-plane, as intended. The electric field amplitude is set to $E_0 = 4 \times 10^6$ V/m, resulting in an induced torque amplitude of approximately $\tau_0 \approx 1 \times 10^{-19}$ N m. This torque is sufficient to overcome the thermal energy $k_{\mathrm{B}}T \approx 4.15 \times 10^{-21}$ J, thereby ensuring that the deterministic electrostatic torque dominates the cluster's response. The angular frequency of the applied field is chosen to be $\omega = 4\pi \times 10^5$ rad/s, which, while providing the desired temporal variations, still maintains electrostatics as an extremely precise approximation.[78] The final state of the cluster is obtained after a trajectory of 10 ms, as shown in Figure 9b. It is evident that the spherical Janus particles are aligned with respect to the electric field's direction in the yz-plane, with any misalignment primarily resulting from the stochastic nature of Brownian motion. It is worth noting

https://doi.org/10.1021/acsomega.4c05669
ACS Omega 2024, 9, 49172−49187

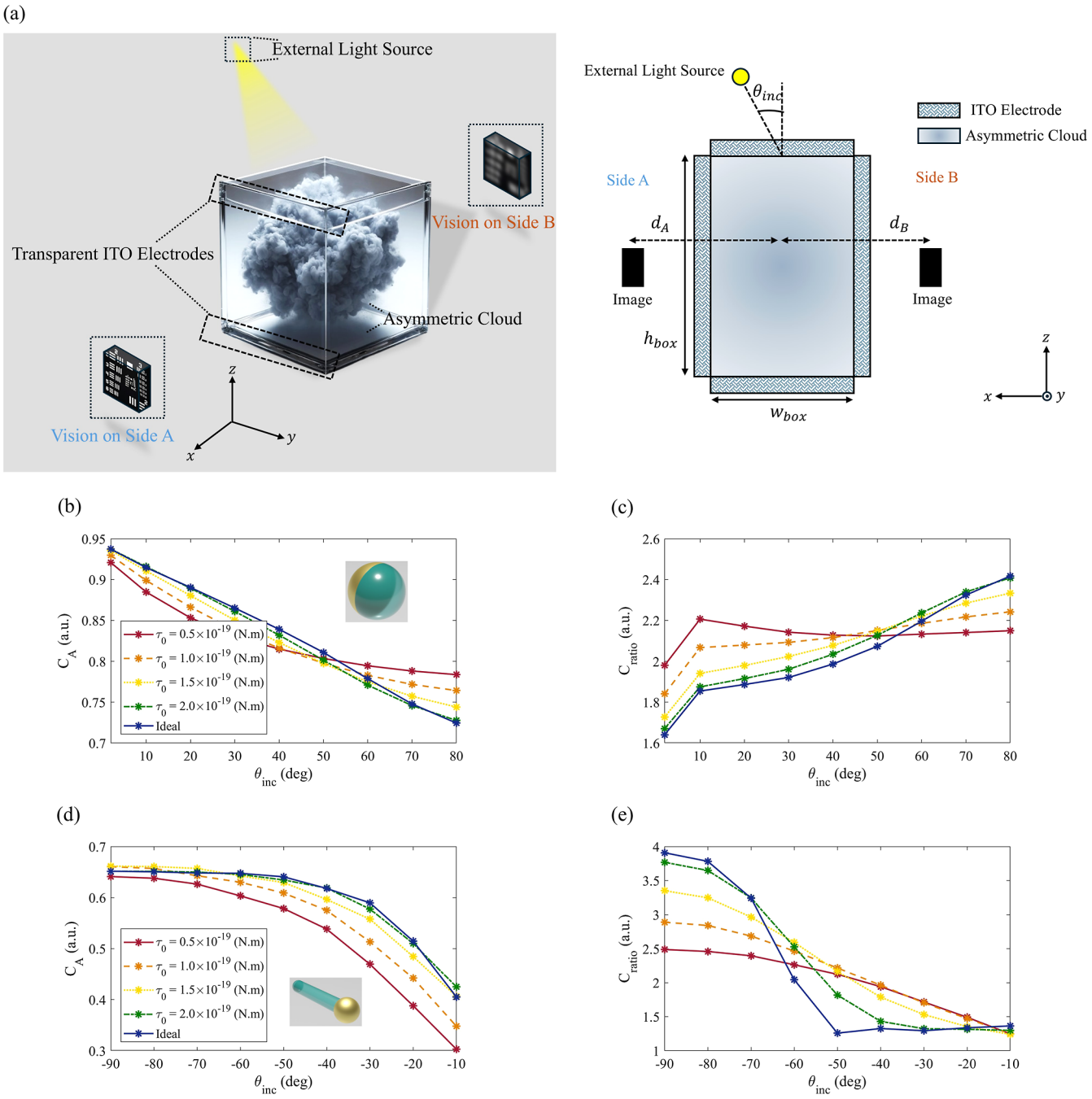

Figure 9. Perspective and cross-sectional depictions of the asymmetric imaging system, containing two images on sides A and B, an asymmetric cloud of the spherical or matchstick-like Janus particles, a CCD to capture images, and an external light source as the main source of noise (a). The contrast on side A (b) and the contrast ratio (c) curves for the spherical Janus particles under the application of various driving torques. The contrast on side A (d) and the contrast ratio (e) plots for matchstick-like particles with different applied torques. These results can serve as the proof of the applicability of the proposed method in this manuscript to control optically asymmetric Janus particles.

that increasing the amplitude of the deterministic electrostatic torque can mitigate this misalignment.

The random initial distribution of 15 matchstick-like Janus particles in air within a cubic box of length $d_b = 10$ μm is depicted in Figure 9c. The background electric field is assumed to be in the form $\mathbf{E}_b = E_0\cos(\omega_b t)\hat{a}_y$, standing for a linear polarization state. As previously demonstrated, the matchstick-like particles naturally align with the direction of the background field, rendering circular polarization unnecessary. Therefore, the background electric field is considered to be linear with an amplitude of $E_0 = 3.7 \times 10^5$ V/m, resulting in an imparted torque with an amplitude of $\tau_0 \approx 1 \times 10^{-19}$ N m, which is sufficiently strong to dominate the stochastic Brownian torque. Due to the linear polarization of the background field, the angular frequency does not play a significant role in this scenario. Nevertheless, for the sake of consistency, it is assumed to be $\omega = 4\pi \times 10^5$ rad/s. The cluster is depicted in its steady state after a transient response of 10 ms in Figure 7d. It is evident that the electrostatic field successfully orients the particles in the yz-plane of the reference frame, aligning them with the direction of the

https://doi.org/10.1021/acsomega.4c05669
ACS Omega 2024, 9, 49172−49187

applied field. The observed misalignment originates from the Brownian random walk of the particles and can be suppressed by strengthening the applied electrostatic field.

To illuminate the final distribution of particles in the *yz*-plane, 200 cluster simulations are conducted for both spherical and matchstick-like Janus particles. The resulting data is then used to fit a probability distribution to the final alignment angle (γ). The results obtained using driving torques with varying strengths for both spherical and matchstick-like particles are illustrated in Figure 7e,f, respectively. It is evident that both types of particles tend to converge to their stable steady states within a confidence interval influenced by Brownian motion. It should also be noted that due to the stochastic nature of Brownian translational and rotational motions, the particles are not fully aligned in other directions ($\alpha \neq \beta \neq 0$). Moreover, increasing the driving torque amplitude will compensate the effects of Brownian motion, which can be observed as sharper peaks in Figure 7. It is also important to mention that the equilibrium angular distributions of the particles can be determined using the Boltzmann function,[73] assuming negligible particle−particle interactions and a dilute dispersion, as described below

$$p(\gamma) \sim e^{-U/k_B T} \tag{21}$$

where U is the potential energy of the particle in the applied electrostatic field. The obtained results can then be utilized to evaluate the accuracy of the numerical simulations (comparisons are provided in the Supporting Information). The obtained probability distributions can be utilized to analyze the asymmetric imaging performance of the aligned particles using the approach based on Monte Carlo simulations proposed in our recently published work.[21]

Prior to introducing the asymmetric imaging setup, interaction of the introduced optically asymmetric Janus particles with light traveling in opposite directions is investigated in Figure 8. It should be noted that the incoming light is considered to be an *x*-polarized plane wave traveling along the $\pm z$-axis for the forward and backward scenarios. Besides, all calculations are performed assuming an incident wave with a wavelength of λ = 590 nm, which lies within the visible range of the electromagnetic spectrum. The polar plots presented in Figure 8a illustrate the far-field gain of the spherical Janus particle for both illumination directions. The gain can be interpreted as the probability of a photon scattering at a particular angle. As shown, in the forward scenario, most photons tend to pass through the particle and scatter in the forward direction, while in the backward scenario, the photons are more likely to be reflected and scatter toward the backward direction. To further clarify the optical performance of the spherical Janus particle, the electric field distribution and far-field gain are illustrated in Figure 8b. As shown, the far-field gain closely follows the electric field pattern, indicating that photons can pass through the particle and travel in the forward direction.

Additionally, for the matchstick-like Janus particle, the far-field gain in both the forward and backward scenarios is depicted in Figure 8c. As shown, in the forward scenario, photons primarily scatter in the forward direction and pass through the particle. In contrast, in the backward scenario, photons are partially reflected, leading to scattering in the backward direction. Furthermore, the electric field distribution and far-field gain of the matchstick-like Janus particle in the forward scenario are illustrated in Figure 8d. As shown, the far-field gain follows the electric field pattern, indicating that photons tend to travel in the forward direction. These results collectively highlight the asymmetric optical properties of the Janus particles studied in our manuscript.

The imaging setup, as shown in Figure 9a, includes an asymmetric cloud containing either the spherical or matchstick-like Janus particles, a target image placed on side A or B, a charge-coupled device (CCD) in order to capture the image, and an illumination light source, which serves as the primary source of noise in the imaging process. The major purpose of asymmetric imaging is to provide a clear vision on side A while obscuring the vision on the other side, which is also referred to as the one-way cloud. In fact, the one-way cloud has the capability to manipulate visibility based on the viewing direction, presenting a strong potential as a replacement for traditional obscurants like smoke, dust, or fog, which block vision from both sides. Due to their inherent asymmetry, optically asymmetric Janus particles can scatter light toward a desired direction, thereby providing the requirements of asymmetric imaging. The cloud is considered to be in a cubic box with equal length and width of w_{box} = 25 cm, and height of h_{box} = 30 cm, surrounded by indium tin oxide (ITO) electrodes in order to provide the electrostatic field for aligning the particles. These dimensions are chosen to resemble an in-lab experiment scale. ITO is a degenerate n-type semiconductor, providing concurrent transparency and conductivity.[79] Therefore, it is a perfect candidate for providing the necessary bias in the asymmetric imaging system. As we have elaborated,[21] the targets on sides A and B are considered to be at the same distance from the cloud ($d_A = d_B$ = 1.5 m) to solely capture the asymmetries imposed by the particles. Moreover, the intensity of the external light source is supposed to be $I_0 = 18P_A = 18P_B$, where P_A and P_B are the image intensities on sides A and B, respectively.

In order to quantify the performance of the asymmetric imaging system, the contrasts of the images seen on sides A and B (C_A and C_B) are calculated using Monte Carlo method for various driving torques.[21] It should be noted that increasing the deterministic electrostatic torque is equivalent to suppressing the stochastic impacts of Brownian motion. Besides, the contrast ratio $\left(C_{ratio} = \frac{C_A}{C_B}\right)$ is a metric to measure the success of the asymmetric imaging procedure by comparing the quality of the images formed on sides A and B. Therefore, one-sided vision can be attained contingent upon maximizing the contrast ratio while maintaining a detectable signal level (C_A) on side A. Considering their fundamental scattering footprints, the spherical and matchstick-like Janus particles are engineered to provide asymmetric imaging under different external light source illumination angles. Specifically, the spherical particles have been shown to be effective while the light source impinges on the cloud from side B, and the matchstick-like particles have been designed to provide the desired asymmetry in case the external light is illuminated from side A. It is essential to notice that in ref 21, the particles are fully aligned in one direction (100% aligned), while here, there are two possible steady states (50% of the particles in each state). Although the particles have been designed to operate at the optimum angle, the particles oriented 180° from the optimum orientation still provide the desired scattering characteristics (high reflection and transmission for the spherical and matchstick-like particles, respectively) to achieve a satisfactory contrast ratio. Hence, even though the proposed

https://doi.org/10.1021/acsomega.4c05669
ACS Omega 2024, 9, 49172−49187

alignment procedure results in two stable equilibrium points, where 50% of the particles are rotated 180°, the one-way cloud is still realizable, as shown in Figure 9, but with a diminished performance compared to the ideal scenario given by ref 21. Under the application of different driving torques, the contrast curves on side A and the contrast ratio plots for the spherical Janus particle are illustrated in Figure 9b,c, respectively. As can be observed, despite the general diminishing in the performance due to the particles' misalignment, it is enhanced around some orientations, as the maximum contrast occurs at angles slightly different from the designed orientations. Furthermore, as mentioned earlier, by increasing the electrostatic torque, both contrast on side A and contrast ratio curves tend toward the ideal scenario, where there exists no stochastic misalignment.

For the matchstick-like Janus particles, the contrast on side A and the contrast ratio curves are shown in Figure 9d,e, respectively. Similar to the spherical particles, although Brownian motion dilutes the overall asymmetric imaging performance, it slightly boosts functionality in certain directions due to the fact that the contrast peaks at other directions rather than the intended angles. Increasing the deterministic torque ameliorates the stochastic impacts of Brownian motion, and the curves converge to the ideal scenario with a sufficiently large electrostatic field application. It should be noted that the mechanical manipulation of the particles within the cluster is vital in achieving the desired asymmetric imaging functionality, which cannot be obtained without suppressing the stochastic impacts of Brownian motion. Finally, although the aforementioned results are presented in the asymmetric imaging context, they provide the proof of the applicability of our proposed approach in a vast range of applications, such as self-assembly, micro- and nanomotors, and drug delivery.

4. CONCLUSION

Meticulous control over the position and orientation of Janus particles within a cluster is substantial in attaining intriguing applications in various advancing fields. However, achieving accessible and precise control remains a significant challenge and an area of active research. In this study, we employed electrostatics to introduce a viable framework for manipulating the orientation of optically asymmetric Janus particles within a cluster. Specifically, we studied the orientation of spherical and matchstick-like objects comprising silica and gold in an ionic environment. We developed a sophisticated multiphysics platform that combines electrostatics with rigid body dynamics, utilizing the boundary element method and the adaptive fast multipole algorithm to explore the transient and steady-state behaviors of the particles. We investigated the electrostatic torques exerted on the particles and their associated potential energies in background media with varying permittivity and ionic strength to elaborate on the stable steady states in the orientation space, emerging as the minima of the potential energy. Our results demonstrated that the particles exhibit two distinct stable equilibrium points, choosing one at random based on their initial orientation. We analyzed the rotational dynamics of a single particle and demonstrated that by adjusting the amplitude and direction of the excitation, we can steer the particle to its target orientation within a specified time frame. We expanded our analysis to align particles within a cluster despite the translation and rotational Brownian motions caused by thermal fluctuations. Our findings revealed that enhancing the deterministic electrostatic torque can effectively mitigate these fluctuations and orient the particles in the desired direction. We then applied our framework to an asymmetric imaging system based on optically asymmetric Janus particles. We demonstrated that our method could successfully overcome the effects of Brownian motion and enable asymmetric vision through the cloud of Janus particles. On top of asymmetric imaging, our proposed method provides a simple, accessible, and effective platform for mechanically manipulating Janus particles in a cluster, which is crucial for various applications such as targeted drug delivery, micro- and nanomotors, and self-assembly. Our approach can be further enhanced by optimizing the spatial distribution of the background electrostatic potential to obtain control over the number of stable equilibrium points, which is the aim of our future research.

■ ASSOCIATED CONTENT

Supporting Information

The Supporting Information is available free of charge at https://pubs.acs.org/doi/10.1021/acsomega.4c05669.

Supporting Information includes: details of the multiphysics platform described in the manuscript; calculation of dipole polarizabilities of particles; numerical verification of the method; validation of the model (PDF)

■ AUTHOR INFORMATION

Corresponding Author

Hossein Mosallaei − *Metamaterials Laboratory, Electrical and Computer Engineering Department, Northeastern University, Boston, Massachusetts 02115, United States*; Email: hosseinm@coe.neu.edu

Authors

Mohammad Mojtaba Sadafi − *Metamaterials Laboratory, Electrical and Computer Engineering Department, Northeastern University, Boston, Massachusetts 02115, United States*; orcid.org/0000-0001-7616-7622

Achiles Fontana da Mota − *Metamaterials Laboratory, Electrical and Computer Engineering Department, Northeastern University, Boston, Massachusetts 02115, United States; Department of Electrical Engineering, University of Brasilia, Brasilia 70910-900, Brazil*

Complete contact information is available at: https://pubs.acs.org/10.1021/acsomega.4c05669

Notes

The authors declare no competing financial interest.

■ ACKNOWLEDGMENTS

This research was developed with funding from the Defense Advanced Research Projects Agency (DARPA). The views, opinions and/or findings expressed are those of the authors and should not be interpreted as representing the official views or policies of the Department of Defense or the U.S. Government. The work has benefited from the support of Northeastern University's Research Computing team by providing resources for high-performance computing through Discovery Cluster.

REFERENCES

(1) Wang, C.; Wu, H.; Chen, Z.; McDowell, M. T.; Cui, Y.; Bao, Z. Self-healing chemistry enables the stable operation of silicon microparticle anodes for high-energy lithium-ion batteries. *Nat. Chem.* **2013**, *5* (12), 1042−1048.

(2) Glover, R. D.; Miller, J. M.; Hutchison, J. E. Generation of metal nanoparticles from silver and copper objects: nanoparticle dynamics on surfaces and potential sources of nanoparticles in the environment. *ACS Nano* **2011**, *5* (11), 8950−8957.

(3) Duan, H.; Wang, D.; Li, Y. Green chemistry for nanoparticle synthesis. *Chem. Soc. Rev.* **2015**, *44* (16), 5778−5792.

(4) De, M.; Ghosh, P. S.; Rotello, V. M. Applications of nanoparticles in biology. *Adv. Mater.* **2008**, *20* (22), 4225−4241.

(5) Salata, O. V. Applications of nanoparticles in biology and medicine. *J. Nanobiotechnol.* **2004**, *2* (1), 3.

(6) Wilczewska, A. Z.; Niemirowicz, K.; Markiewicz, K. H.; Car, H. Nanoparticles as drug delivery systems. *Pharmacol. Rep.* **2012**, *64* (5), 1020−1037.

(7) Cardoso, V. F.; Francesko, A.; Ribeiro, C.; Bañobre-López, M.; Martins, P.; Lanceros-Mendez, S. Advances in magnetic nanoparticles for biomedical applications. *Adv. Healthcare Mater.* **2018**, *7* (5), 1700845.

(8) Zhang, N.; Han, C.; Xu, Y.-J.; Foley, J. J., IV; Zhang, D.; Codrington, J.; Gray, S. K.; Sun, Y. Near-field dielectric scattering promotes optical absorption by platinum nanoparticles. *Nat. Photonics* **2016**, *10* (7), 473−482.

(9) Barati Sedeh, H.; Pires, D. G.; Chandra, N.; Gao, J.; Tsvetkov, D.; Terekhov, P.; Kravchenko, I.; Litchinitser, N. Manipulation of scattering spectra with topology of light and matter. *Laser Photonics Rev.* **2023**, *17* (3), 2200472.

(10) Mueller, N. S.; Okamura, Y.; Vieira, B. G.; Juergensen, S.; Lange, H.; Barros, E. B.; Schulz, F.; Reich, S. Deep strong light−matter coupling in plasmonic nanoparticle crystals. *Nature* **2020**, *583* (7818), 780−784.

(11) Barati Sedeh, H.; Litchinitser, N. M. Singular optics empowered by engineered optical materials. *Nanophotonics* **2023**, *12* (14), 2687−2716.

(12) Sadafi, M. M.; da Mota, A. F.; Mosallaei, H. Dynamic control of light scattering in a single particle enabled by time modulation. *Appl. Phys. Lett.* **2023**, *123* (10), 101702.

(13) Sadafi, M. M.; Karami, H.; Hosseini, M. A tunable hybrid graphene-metal metamaterial absorber for sensing in the thz regime. *Curr. Appl. Phys.* **2021**, *31*, 132−140.

(14) Zhang, T.; Lyu, D.; Xu, W.; Feng, X.; Ni, R.; Wang, Y. Janus particles with tunable patch symmetry and their assembly into chiral colloidal clusters. *Nat. Commun.* **2023**, *14* (1), 8494.

(15) Roh, K.-H.; Martin, D. C.; Lahann, J. Biphasic janus particles with nanoscale anisotropy. *Nat. Mater.* **2005**, *4* (10), 759−763.

(16) Walther, A.; Muller, A. H. Janus particles: synthesis, self-assembly, physical properties, and applications. *Chem. Rev.* **2013**, *113* (7), 5194−5261.

(17) Tao, S.; Lin, B.; Zhou, H.; Sha, S.; Hao, X.; Wang, X.; Chen, J.; Zhang, Y.; Pan, J.; Xu, J.; et al. Janus particle-engineered structural lipiodol droplets for arterial embolization. *Nat. Commun.* **2023**, *14* (1), 5575.

(18) Chen, Y.; Chen, Z.; Wei, J. Fe3o4 nanoparticle-based janus photonic crystal microbeads with multiple fluorescence colors for information coding. *ACS Appl. Nano Mater.* **2023**, *6* (16), 14702−14709.

(19) Peng, L.; Wang, Z. L.; Cao, X.; Zhang, L. From janus triboelectric interface to energy-autonomous sensing system: An asymmetric design. *Nano Energy* **2024**, *120*, 109146.

(20) Kruk, S. S.; Wang, L.; Sain, B.; Dong, Z.; Yang, J.; Zentgraf, T.; Kivshar, Y. Asymmetric parametric generation of images with nonlinear dielectric metasurfaces. *Nat. Photonics* **2022**, *16* (8), 561−565.

(21) da Mota, A. F.; Sadafi, M. M.; Mosallaei, H. Asymmetric imaging through engineered janus particle obscurants using a monte carlo approach for highly asymmetric scattering media. *Sci. Rep.* **2024**, *14* (1), 3850.

(22) Guo, S.; Boyarsky, M.; Vigil, S. A.; Yu, Y.; Moreno-Hernandez, I. A.; Gehm, M. E.; Wiley, B. J. Toward one-way smoke: Synthesis of copper-based microclubs with asymmetric scattering and absorption. *Adv. Funct. Mater.* **2024**, *34*, 2315289.

(23) Shao, D.; Li, J.; Zheng, X.; Pan, Y.; Wang, Z.; Zhang, M.; Chen, Q.-X.; Dong, W.-F.; Chen, L. Janus "nano-bullets" for magnetic targeting liver cancer chemotherapy. *Biomaterials* **2016**, *100*, 118−133.

(24) Tang, S.; Zhang, F.; Gong, H.; Wei, F.; Zhuang, J.; Karshalev, E.; Esteban-Fernández de Ávila, B.; Huang, C.; Zhou, Z.; Li, Z.; et al. Enzyme-powered janus platelet cell robots for active and targeted drug delivery. *Sci. Robot.* **2020**, *5* (43), No. eaba6137.

(25) Ilic, O.; Kaminer, I.; Zhen, B.; Miller, O. D.; Buljan, H.; Soljačić, M. Topologically enabled optical nanomotors. *Sci. Adv.* **2017**, *3* (6), No. e1602738.

(26) Jiang, S.; Li, B.; Zhao, J.; Wu, D.; Zhang, Y.; Zhao, Z.; Zhang, Y.; Yu, H.; Shao, K.; Zhang, C.; et al. Magnetic janus origami robot for cross-scale droplet omni-manipulation. *Nat. Commun.* **2023**, *14* (1), 5455.

(27) Chen, Q.; Bae, S. C.; Granick, S. Directed self-assembly of a colloidal kagome lattice. *Nature* **2011**, *469* (7330), 381−384.

(28) Hessberger, T.; Braun, L. B.; Zentel, R. Interfacial self-assembly of amphiphilic dual temperature responsive actuating janus particles. *Adv. Funct. Mater.* **2018**, *28* (21), 1800629.

(29) Tkachenko, G.; Truong, V. G.; Esporlas, C. L.; Sanskriti, I.; Nic Chormaic, S. Evanescent field trapping and propulsion of janus particles along optical nanofibers. *Nat. Commun.* **2023**, *14* (1), 1691.

(30) Valdez-Garduño, M.; Leal-Estrada, M.; Oliveros-Mata, E. S.; Sandoval-Bojorquez, D. I.; Soto, F.; Wang, J.; Garcia-Gradilla, V. Density asymmetry driven propulsion of ultrasound-powered janus micromotors. *Adv. Funct. Mater.* **2020**, *30* (50), 2004043.

(31) Lee, J.-Y.; Alú, A.; Deravi, L. F. Enabling rotation over electrophoretic motion in janus particles under applied electric field. *Appl. Phys. Lett.* **2024**, *124* (2), 024101.

(32) Sofer, D.; Yossifon, G.; Miloh, T. Electro-orientation and electro-rotation of metallodielectric janus particles. *Langmuir* **2023**, *39* (2), 790−799.

(33) Sadafi, M. M.; Taghavi, M.; da Mota, A. F.; Mosallaei, H. Optical manipulation of nanoparticles: A selective excitation approach using highly focused orbital angular momentum beams. *Adv. Photonics Res.* **2023**, *4*, 2200224.

(34) Rodríguez-Fortuño, F. J.; Engheta, N.; Martínez, A.; Zayats, A. V. Lateral forces on circularly polarizable particles near a surface. *Nat. Commun.* **2015**, *6* (1), 8799.

(35) Taghavi, M.; Salary, M. M.; Mosallaei, H. Multifunctional metasails for self-stabilized beam-riding and optical communication. *Nanoscale Adv.* **2022**, *4* (7), 1727−1740.

(36) Taghavi, M.; Mosallaei, H. Increasing the stability margins using multi-pattern metasails and multi-modal laser beams. *Sci. Rep.* **2022**, *12* (1), 20034.

(37) Krishnan, M.; Mojarad, N.; Kukura, P.; Sandoghdar, V. Geometry-induced electrostatic trapping of nanometric objects in a fluid. *Nature* **2010**, *467* (7316), 692−695.

(38) Jin, Y.; Xu, W.; Zhang, H.; Li, R.; Sun, J.; Yang, S.; Liu, M.; Mao, H.; Wang, Z. Electrostatic tweezer for droplet manipulation. *Proc. Natl. Acad. Sci. U.S.A.* **2022**, *119* (2), No. e2105459119.

(39) Tae Kim, J.; Spindler, S.; Sandoghdar, V. Scanning-aperture trapping and manipulation of single charged nanoparticles. *Nat. Commun.* **2014**, *5* (1), 3380.

(40) Mou, F.; Xie, Q.; Liu, J.; Che, S.; Bahmane, L.; You, M.; Guan, J. Zno-based micromotors fueled by co2: the first example of self-reorientation-induced biomimetic chemotaxis. *Natl. Sci. Rev.* **2021**, *8* (11), nwab066.

(41) Chen, C.; Mou, F.; Xu, L.; Wang, S.; Guan, J.; Feng, Z.; Wang, Q.; Kong, L.; Li, W.; Wang, J.; et al. Semiconductors: Light-steered isotropic semiconductor micromotors. *Adv. Mater.* **2017**, *29* (3), 201603374.

https://doi.org/10.1021/acsomega.4c05669
ACS Omega 2024, 9, 49172−49187

(42) Che, S.; Zhang, J.; Mou, F.; Guo, X.; Kauffman, J. E.; Sen, A.; Guan, J. Light-programmable assemblies of isotropic micromotors. *Research* **2022**, *2022*, 9816562.
(43) Fogolari, F.; Brigo, A.; Molinari, H. The poisson−boltzmann equation for biomolecular electrostatics: a tool for structural biology. *J. Mol. Recognit.* **2002**, *15* (6), 377−392.
(44) Baker, N. A. Poisson−Boltzmann Methods for Biomolecular Electrostatics. *Methods Enzymol.* **2004**, *383*, 94−118.
(45) Gilson, M. K.; Davis, M. E.; Luty, B. A.; McCammon, J. A. Computation of electrostatic forces on solvated molecules using the poisson-boltzmann equation. *J. Phys. Chem.* **1993**, *97* (14), 3591−3600.
(46) Tsao, H.-K. Counterion distribution enclosed in a cylinder and a sphere. *J. Phys. Chem. B* **1998**, *102* (50), 10243−10247.
(47) Saboorian-Jooybari, H.; Chen, Z. Analytical solutions of the poisson-boltzmann equation within an interstitial electrical double layer in various geometries. *Chem. Phys.* **2019**, *522*, 147−162.
(48) Nicholls, A.; Honig, B. A rapid finite difference algorithm, utilizing successive over-relaxation to solve the poisson−boltzmann equation. *J. Comput. Chem.* **1991**, *12* (4), 435−445.
(49) Luty, B. A.; Davis, M. E.; McCammon, J. A. Solving the finite-difference non-linear poisson−boltzmann equation. *J. Comput. Chem.* **1992**, *13* (9), 1114−1118.
(50) Cortis, C. M.; Friesner, R. A. Numerical solution of the poisson−boltzmann equation using tetrahedral finite-element meshes. *J. Comput. Chem.* **1997**, *18* (13), 1591−1608.
(51) Shestakov, A.; Milovich, J.; Noy, A. Solution of the nonlinear poisson−boltzmann equation using pseudo-transient continuation and the finite element method. *J. Colloid Interface Sci.* **2002**, *247* (1), 62−79.
(52) Boschitsch, A. H.; Fenley, M. O.; Zhou, H.-X. Fast boundary element method for the linear poisson- boltzmann equation. *J. Phys. Chem. B* **2002**, *106* (10), 2741−2754.
(53) Bordner, A. J.; Huber, G. Boundary element solution of the linear poisson−boltzmann equation and a multipole method for the rapid calculation of forces on macromolecules in solution. *J. Comput. Chem.* **2003**, *24* (3), 353−367.
(54) Lu, B.; Zhang, D.; McCammon, J. A. Computation of electrostatic forces between solvated molecules determined by the poisson−boltzmann equation using a boundary element method. *J. Chem. Phys.* **2005**, *122* (21), 214102.
(55) Fogolari, F.; Zuccato, P.; Esposito, G.; Viglino, P. Biomolecular electrostatics with the linearized poisson-boltzmann equation. *Biophys. J.* **1999**, *76* (1), 1−16.
(56) Hsu, J.-P.; Liu, B.-T. Exact solution to the linearized poisson−boltzmann equation for spheroidal surfaces. *J. Colloid Interface Sci.* **1996**, *178* (2), 785−788.
(57) Lu, B.; Cheng, X.; Huang, J.; McCammon, J. A. An adaptive fast multipole boundary element method for poisson- boltzmann electrostatics. *J. Chem. Theory Comput.* **2009**, *5* (6), 1692−1699.
(58) Boschitsch, A. H.; Fenley, M. O. A fast and robust poisson−boltzmann solver based on adaptive cartesian grids. *J. Chem. Theory Comput.* **2011**, *7* (5), 1524−1540.
(59) Wang, B.; Zhang, W.; Cai, W. Fast multipole method for 3-d poisson-boltzmann equation in layered electrolyte-dielectric media. *J. Comput. Phys.* **2021**, *439*, 110379.
(60) Lu, B.; Cheng, X.; Hou, T.; McCammon, J. A. Calculation of the maxwell stress tensor and the poisson-boltzmann force on a solvated molecular surface using hypersingular boundary integrals. *J. Chem. Phys.* **2005**, *123* (8), 084904.
(61) Xiao, L.; Cai, Q.; Ye, X.; Wang, J.; Luo, R. Electrostatic forces in the poisson-boltzmann systems. *J. Chem. Phys.* **2013**, *139* (9), 094106.
(62) Taghavi, M.; Sabri, R.; Mosallaei, H. Active metasurfaces for non-rigid light sail interstellar optical communication. *Adv. Theory Simul.* **2024**, *7* (1), 2300359.
(63) Altmann, S. L. *Rotations, Quaternions, and Double Groups*; Courier Corporation, 2005; .
(64) Betsch, P.; Siebert, R. Rigid body dynamics in terms of quaternions: Hamiltonian formulation and conserving numerical integration. *Int. J. Numer. Methods Eng.* **2009**, *79* (4), 444−473.
(65) Stillinger, F. H., Jr. Interfacial solutions of the poisson-boltzmann equation. *J. Chem. Phys.* **1961**, *35* (5), 1584−1589.
(66) Altman, M. D.; Bardhan, J. P.; White, J. K.; Tidor, B. Accurate solution of multi-region continuum biomolecule electrostatic problems using the linearized poisson−boltzmann equation with curved boundary elements. *J. Comput. Chem.* **2009**, *30* (1), 132−153.
(67) Favro, L. D. Theory of the rotational brownian motion of a free rigid body. *Phys. Rev.* **1960**, *119* (1), 53−62.
(68) Delong, S.; Balboa Usabiaga, F.; Donev, A. Brownian dynamics of confined rigid bodies. *J. Chem. Phys.* **2015**, *143* (14), 144107.
(69) Hubbard, P. S. Rotational brownian motion. *Phys. Rev. A* **1972**, *6* (6), 2421−2433.
(70) Azadjou, H.; Błażkiewicz, M.; Erwin, A.; Valero-Cuevas, F. J. Dynamical analyses show that professional archers exhibit tighter, finer and more fluid dynamical control than neophytes. *Entropy* **2023**, *25* (10), 1414.
(71) Diebel, J. Representing attitude: Euler angles, unit quaternions, and rotation vectors. *Matrix* **2006**, *58* (15−16), 1−35.
(72) Jones, T. B. *Electromechanics of Particles*; Cambridge University Press, 1995; .
(73) Rosensweig, R. E. *Ferrohydrodynamics*; Courier Corporation, 1997; .
(74) Kjellander, R. Decay behavior of screened electrostatic surface forces in ionic liquids: the vital role of non-local electrostatics. *Phys. Chem. Chem. Phys.* **2016**, *18* (28), 18985−19000.
(75) Gebbie, M. A.; Dobbs, H. A.; Valtiner, M.; Israelachvili, J. N. Long-range electrostatic screening in ionic liquids. *Proc. Natl. Acad. Sci. U.S.A.* **2015**, *112* (24), 7432−7437.
(76) Kubo, R. The fluctuation-dissipation theorem. *Rep. Prog. Phys.* **1966**, *29* (1), 255−284.
(77) Prost, J.; Joanny, J.-F.; Parrondo, J. M. Generalized fluctuation-dissipation theorem for steady-state systems. *Phys. Rev. Lett.* **2009**, *103* (9), 090601.
(78) Jackson, J. D. *Classical Electrodynamics*; John Wiley and Sons, 1999; .
(79) Yu, Z.; Perera, I. R.; Daeneke, T.; Makuta, S.; Tachibana, Y.; Jasieniak, J. J.; Mishra, A.; Bäuerle, P.; Spiccia, L.; Bach, U. Indium tin oxide as a semiconductor material in efficient p-type dye-sensitized solar cells. *NPG Asia Mater.* **2016**, *8* (9), No. e305.

https://doi.org/10.1021/acsomega.4c05669
ACS Omega 2024, 9, 49172−49187